Flow topology dynamics in a three-dimensional phase space for turbulent Rayleigh-Bénard convection

F. Dabbagh,[1,2,*] F. X. Trias,[1,†] A. Gorobets,[3,‡] and A. Oliva[1,§]

[1]*Heat and Mass Transfer Technological Center, ESEIAAT, Technical University of Catalonia, c/Colom 11, 08222 Terrassa, Barcelona, Spain*

[2]*Christian Doppler Laboratory for Multi-Scale Modeling of Multiphase Processes, Johannes Kepler University, Altenbergerstraße 69, 4040 Linz, Austria*

[3]*Keldysh Institute of Applied Mathematics of Russian Academy of Sciences, 4A Miusskaya Square, Moscow 125047, Russia*

(Received 12 April 2019; accepted 28 January 2020; published 28 February 2020)

We study the flow topology dynamics in terms of the paramount nonlinearities of enstrophy and strain production at hard turbulent regimes of Rayleigh-Bénard convection (RBC). To do so, a data set of direct numerical simulations for air turbulent RBC at Rayleigh numbers $\mathrm{Ra} = \{10^8, 10^{10}, 10^{11}\}$ is analyzed. Considering the bulk dynamics therein, the classical two-dimensional mean Lagrangian evolution of Q_G and R_G invariants of $\mathsf{G} \equiv \nabla \boldsymbol{u}$ is extended to three dimensions by decomposing R_G into two parts: the strain production R_S and the enstrophy production $\mathrm{tr}(\Omega^2\mathsf{S})$. In this way, the three-dimensional phase space $(Q_\mathsf{G}, R_\mathsf{S}, \mathrm{tr}(\Omega^2\mathsf{S}))$ allows us to identify separately the nonlinear straining and rotational mechanisms in turbulence. The main resultant observations attest that, when the turbulent regime is notably hard, a rising local self-amplification of the velocity gradient takes place in strain-dominated areas. This process is strongly aided by vortex contraction. Concomitantly, a pronounced increase in the linear contributions of vortex stretching is also identified, particularly relevant to strain-dominated slots.

DOI: 10.1103/PhysRevFluids.5.024603

I. INTRODUCTION

Many circulations in nature and industry, such as convection in the outer layer of the Sun, coherent structures in the Earth's atmosphere and oceans, mantle convection in the Earth's core, and circulation in nuclear reactors and in solar thermal power plants, are ruled by Rayleigh-Bénard convection (RBC). Namely, the turbulent dynamics therein mainly stems from buoyancy variations in the dynamo of a thermally driven flow heated from below and cooled from above [1–3]. Besides the onset of flow structures, this dynamics becomes of significant complexity when the grade of turbulence and thermal forcing is very high, i.e., Rayleigh number $\mathrm{Ra} > 10^{10}$. For instance, the rising self-sustained instabilities of RBC induce augmenting countergradient diffusion and energetic nonequilibrium between the buoyant production and viscous dissipation, which are mainly compensated by pressure fluctuations [4,5]. Although important features have been explored using direct numerical simulation (DNS) of RBC at hard turbulent regimes [6,7], such as the stable boundary layers at $\mathrm{Ra} = 2 \times 10^{12}$ [8] and the thermal plumes statistics at $\mathrm{Ra} = 10^{12}$ [9], many

*firas.dabbagh@jku.at
†xavi@cttc.upc.edu
‡andrey.gorobets@gmail.com
§oliva@cttc.upc.edu

questions regarding the coherent (small-scale) structures remain. For instance, there is a lack of understanding about the flow topology and small-scale dynamics even though these components have a crucial contribution to the turbulent wind and energy budgets. They fully compose the main turbulence mechanisms, such as the evolution of hairpin vorticity dynamics, the non-Gaussianity, the strain and dissipation production, and the cascade of kinetic energy [10–12]. In this regard, we aim to shed light on the following research question: How do the physically meaningful nonlinearities, such as the enstrophy generation (mechanism of vortex stretching) and the strain and dissipation production (mechanism of kinetic energy cascade), behave at hard turbulent regimes of RBC? The enstrophy and strain production terms constitute the key elements responsible for the self-amplifying nature of the velocity derivative $\mathsf{G} \equiv \nabla \boldsymbol{u}$ in turbulence, which is believed to be a universal feature [10]. The role of G properties is remarkable in investigating the structures of turbulent fluid motions [13] and the fine-scale dynamics [14,15]. Another important relation in this regard is the so-called Tennekes-Lumely balance [11], which states that for statistically stationary turbulence at high Reynolds numbers the viscous and production terms of enstrophy are in balance. Therefore, a detailed analysis of the small-scale motions during their lifetime, in terms of these nonlinearities, can provide fundamental perspectives about how thermal turbulence is evolving with Ra in RBC. Moreover, apart from improving our understanding of buoyancy-driven turbulence, it can also provide highly valuable information needed to develop better turbulence models [16,17].

In this paper we first outline a short description of the DNS configuration in Sec. II, together with an overview of previous findings regarding flow topology and small-scale dynamics for turbulent RBC at $\mathrm{Ra} = \{10^8, 10^{10}\}$, reported in Ref. [18]. In particular, we focus on showing the counterparts encountered at a different turbulence grade at $\mathrm{Ra} = 10^{11}$. Afterward, the total group of the DNS data set, i.e., $\mathrm{Ra} = \{10^8, 10^{10}, 10^{11}\}$, is used to explore the small-scale dynamics in terms of the enstrophy and strain production terms in Sec. III. Then, in order to have a more complete picture, the dynamics of small-scale kinetic-thermal interactions is studied in Sec. IV. Finally, all relevant results are summarized and conclusions are given in Sec. V.

II. BACKGROUND

In the above-explained context, well-known features of the small turbulent scales already encountered in different kinds of turbulent flows, e.g., isotropic turbulence [15], turbulent boundary layer (BL) [19], channel flow [20], turbulent mixing layer [21], and turbulent jets [22], were first explored in RBC by Dabbagh *et al.* [18] using DNS results at $\mathrm{Ra} = \{10^8, 10^{10}\}$. Namely, we simulated the dimensionless incompressible Navier-Stokes (NS) and thermal energy equations given by

$$\frac{D\boldsymbol{u}}{Dt} = \sqrt{\frac{\mathrm{Pr}}{\mathrm{Ra}}}\nabla^2\boldsymbol{u} - \nabla p + \boldsymbol{f}, \quad \nabla \cdot \boldsymbol{u} = 0, \tag{1}$$

$$\frac{DT}{Dt} = \frac{1}{\sqrt{\mathrm{Ra}\,\mathrm{Pr}}}\nabla^2 T, \tag{2}$$

where $D/Dt = \partial/\partial t + \boldsymbol{u} \cdot \nabla$ is the Lagrangian derivative with time t, p is the pressure, T is the temperature, and $\boldsymbol{u} = (u, v, w)$ is the velocity field in Cartesian coordinates $\boldsymbol{x} = (x, y, z)$. The governing equations (1) and (2) are written in nondimensional form using the cavity height H, the temperature difference between the upper and lower walls $\Delta\Theta$, and the buoyant velocity $U_{\mathrm{ref}} = \sqrt{\alpha g H \Delta\Theta}$ as references, where α is the volumetric thermal expansion coefficient and g is the gravitational acceleration. The Boussinesq approximation is used to model the buoyancy forces, i.e., $\boldsymbol{f} = (0, T, 0)$. The configuration studied is shown in Fig. 1(a). Considering that the cavity is filled with air ($\mathrm{Pr} = \nu/\kappa = 0.7$), then the system depends only on the Rayleigh number $\mathrm{Ra} = g\alpha\Delta\Theta H^3/\nu\kappa$, where ν is the kinematic viscosity and κ is the thermal diffusivity. The global

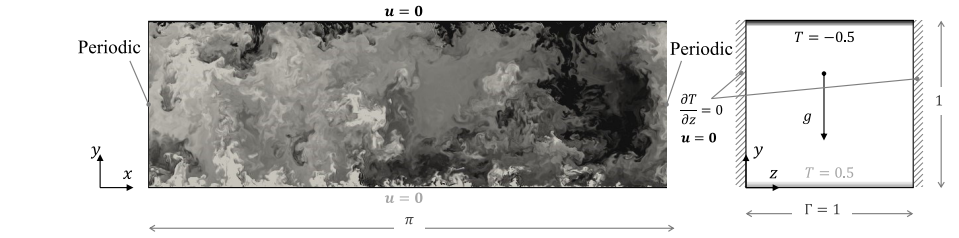

(a)

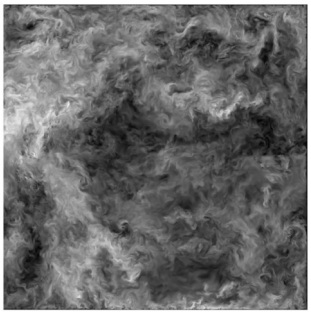

(b)

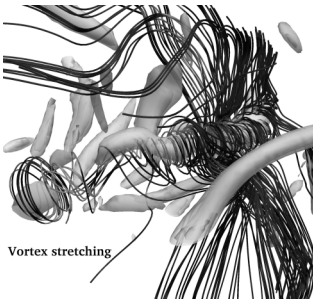

(c)

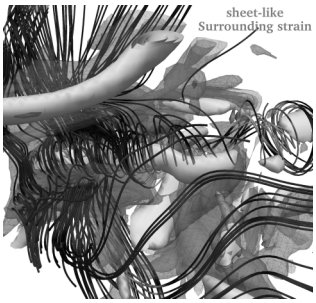

(d)

FIG. 1. (a) Schema of the Rayleigh-Bénard configuration studied in Refs. [16,18] and rendered with an instantaneous temperature field developed from the DNS at $\mathrm{Ra} = 10^{10}$. (b) Instantaneous picture of $|\boldsymbol{u}|$ at $\mathrm{Ra} = 10^{11}$ for a spanwise cross section. (c) Structures of high positive Q_{G} isocontours, which are arranged like worms of intensive enstrophy. (d) Same as in (c) in addition to visualization of the sheetlike strain structures that follow high negative values of Q_{G}. Both (c) and (d) are taken from the DNS results at $\mathrm{Ra} = 10^8$ and supplemented with some streamlines.

response is measured via the average Nusselt number Nu given by

$$\mathrm{Nu} = \sqrt{\mathrm{Ra}\,\mathrm{Pr}}\langle vT\rangle_A - \frac{\partial\langle T\rangle_A}{\partial y}, \tag{3}$$

where the operator in angular brackets represents the temporal average (likewise it denotes the ensemble average in the statistical analysis) and the subscript A refers to the average over a horizontal x-z plane at a given y position. For details about the used numerical methods, algorithms, and verification of the DNS results, the reader is referred to our previous work [18]. In this work we extend our DNS set with a simulation at $\mathrm{Ra} = 10^{11}$, computed on 8192 CPU cores of the MareNostrum 4 supercomputer [23], and using the in-house STG code [24] on a grid of 5.7×10^9 nodes [see Fig. 1(b) and Table I for details]. Similarly to the previous DNS [18], a fourth-order symmetry-preserving spatial discretization [25] has been used together with a self-adaptive second-order explicit time-integration scheme [26]. Finally, herein, the total data set of DNS results at $\mathrm{Ra} = \{10^8, 10^{10}, 10^{11}\}$ is considered and analyzed, and a summary of parameters is given in Table I. The power-law scaling obtained, $\mathrm{Nu} \sim \mathrm{Ra}^{0.31}$, agrees very well with the fit of Grossmann-Lohse theory from Stevens *et al.* [27] and the DNS results of van der Poel *et al.* [9] for an air-filled cylindrical cell of aspect ratio 1/3 and Ra up to 10^{12}.

As mentioned above, results at $\mathrm{Ra} = \{10^8, 10^{10}\}$ allowed us to study relevant features of the small turbulent scales in RBC [18]. For example, we clearly observed the universal inclined teardrop shape of the joint PDF of the second, $Q_{\mathsf{G}} = -1/2\,\mathrm{tr}(\mathsf{G}^2)$, and third, $R_{\mathsf{G}} = -1/3\,\mathrm{tr}(\mathsf{G}^3)$, invariant of the velocity gradient tensor G in the two-dimensional (2D) phase space $(Q_{\mathsf{G}}, R_{\mathsf{G}})$ [see the similar tendency at $\mathrm{Ra} = 10^{11}$ in Fig. 2(a)]. Notice that the flow is solenoidal; therefore, the first invariant

TABLE I. Physical and numerical parameters of the simulation adopted with refinement approaches to the Grötzbach estimate $\eta_{\text{Grö}} \leqslant \pi\,\text{Pr}^{1/2}[(\text{Nu}-1)\text{Ra}]^{-1/4}$ [28]. Here $\eta_{\text{DNS}} = (\Delta x \Delta y \Delta z)^{1/3}_{\text{max}}$ identifies the DNS grid size with N_{BL} as the imposed number of nodes inside the thermal boundary layers (exceeding Shishkina *et al.* [29] requirements). In addition, Δt represents the time step in free-fall time units (TU) and ζ indicates the temporal integration periods that guarantee a statistically stable turbulent heat transport. Quantitatively, ζ_{st} lasts for several large-eddy turnover times τ_{eddy} during which consecutive snapshots are gathered for the statistical analysis. Using the definition of $\tau_{\text{eddy}} = H/\boldsymbol{u}_{\text{rms}}$, where $\boldsymbol{u}_{\text{rms}}$ is the root mean square of the bulk velocity, $\tau_{\text{eddy}} \approx \{7, 5, 4\}$ TU for $\text{Ra} = \{10^8, 10^{10}, 10^{11}\}$, respectively.

Ra	$\eta_{\text{Grö}}$	$\frac{(\Delta y=\Delta z)_{\text{max}}}{\eta_{\text{Grö}}}$	$\frac{\Delta x}{\Delta y_{\text{max}}}$	η_{DNS}	$N_x \times N_y \times N_z$	N_{BL}	Δt (TU)	ζ (TU)	$\zeta_{\text{st}}[\tau_{\text{eddy}}]$	Nu
10^8	0.0109	0.70	1.0	7.70×10^{-3}	$400 \times 208 \times 208$	9	1.45×10^{-3}	500	40	30.9
10^{10}	0.00246	0.92	1.36	2.50×10^{-3}	$1024 \times 768 \times 768$	12	4.14×10^{-4}	200	10	128.1
10^{11}	0.00114	0.93	1.44	1.20×10^{-3}	$2048 \times 1662 \times 1662$	13	1.66×10^{-4}	165	10	269.5

is zero, i.e., $P_{\mathsf{G}} = \text{tr}(\mathsf{G}) = \boldsymbol{\nabla} \cdot \boldsymbol{u} = 0$. It is very common to use this phase space to classify the flow topology into four different classes [13,15]. Namely, $R_{\mathsf{G}} < 0$ and $Q_{\mathsf{G}} \gg 0$ correspond to stable tubelike vortex-stretching structures, where positive enstrophy production is prevalent [see the instantaneous visualization in Fig. 1(c) for the high positive Q_{G} isosurfaces at $\text{Ra} = 10^8$, which are structured as the so-called worms [10], together with the streamlines]. In the opposite quadrant, when $R_{\mathsf{G}} > 0$ and $Q_{\mathsf{G}} \ll 0$, the straining production becomes dominant and it is mostly associated with strong unstable sheetlike viscous dissipative structures [the additional visualization shown in Fig. 1(d) that exposes the surrounding sheetlike strain, which is characterized by high negative values of Q_{G}]. The other two less frequent quadrants correspond, respectively, to ribbons of unstable vortex-compressing structures ($Q_{\mathsf{G}} \gg 0$ and $R_{\mathsf{G}} > 0$) and highly dissipative tubelike-shape structures ($Q_{\mathsf{G}} < 0$ and $R_{\mathsf{G}} < 0$, below the null-discriminant curve $D_{\mathsf{G}} = \frac{27}{4}R_{\mathsf{G}}^2 + Q_{\mathsf{G}}^3 = 0$). In general, the joint probability density function (PDF) aspect rendered in Fig. 2(a) indicates that most of the flow domain is occupied by large-scale (small mean gradients) dynamics around the origin, while the turbulent small-scale motions obey substantially the tubelike vortex-stretching and the sheetlike viscous dissipation structures. The life cycle of these scales, on the other hand, was interpreted by studying the mean evolution of Q_{G} and R_{G} invariants in the same $(Q_{\mathsf{G}}, R_{\mathsf{G}})$ phase space, meaning

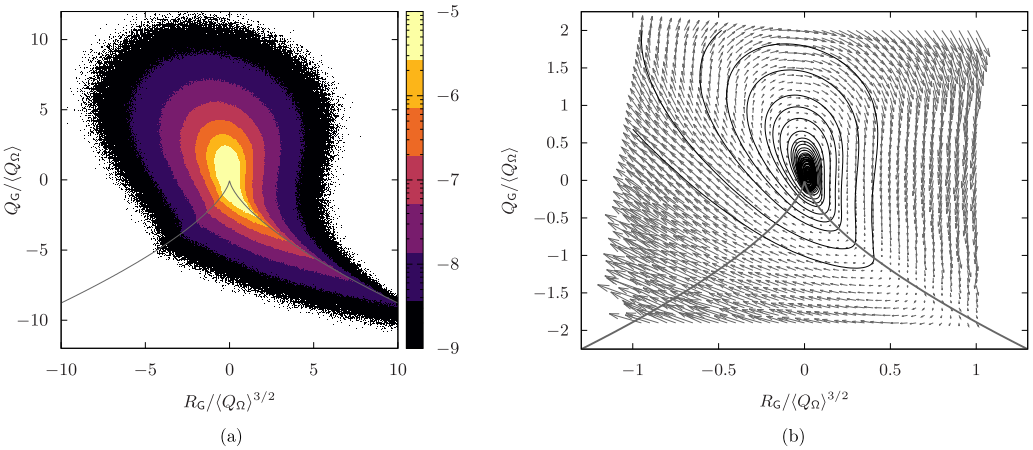

FIG. 2. (a) Joint PDF of normalized Q_{G} and R_{G} invariants in their own space, rendered on a logarithmic scale, and (b) conditional mean vectors of $\langle DQ_{\mathsf{G}}/Dt\rangle$ and $\langle DR_{\mathsf{G}}/Dt\rangle$ in the same plane together with the integral trajectories (black solid orbits). Both outcomes are taken from $\text{Ra} = 10^{11}$, through the bulk, where the solid continuous gray lines indicate the null-discriminant curve $D_{\mathsf{G}} = 0$.

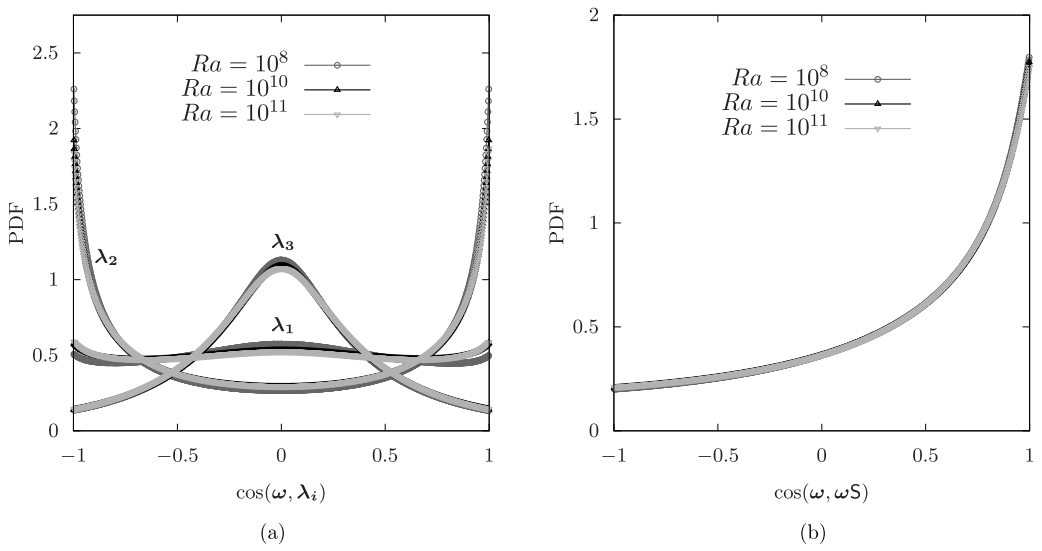

FIG. 3. PDF of vorticity alignments with the eigenvectors of (a) the rate-of-strain tensor and (b) the vortex-stretching vector $\boldsymbol{\omega}\mathsf{S}$, through the bulk, at Ra $= \{10^8, 10^{10}, 10^{11}\}$.

that, in the frame of a moving observer following a fluid particle, the local surrounding flow structures are essentially described by G and its invariants, i.e., Q_G and R_G. Its change in time can be depicted by the Lagrangian dynamics of invariant quantities as proposed by Martín *et al.* [14] and Ooi *et al.* [15]. So, identical to that procedure, the mean trajectories of $(\langle DQ_\mathsf{G}/Dt\rangle, \langle DR_\mathsf{G}/Dt\rangle)$ were studied in RBC [18] and revealed the similar (universal?) characteristic clockwise spiraling behavior decaying towards the origin [see the planer cycling trajectories plotted for Ra $= 10^{11}$ in Fig. 2(b)]. From Fig. 2(b) one can perceive how the local flow topology is altering, during its lifetime, from the viscous dissipation to the vortex stretching and then the compressing structures, before vanishing in the mean.

Apart from the above attributes, we also observed in Ref. [18] the preferential alignment of vorticity $\boldsymbol{\omega} = \boldsymbol{\nabla} \times \boldsymbol{u}$ with the intermediate eigenstrain vector $\boldsymbol{\lambda}_2$ and the vortex-stretching vector $\boldsymbol{\omega}\mathsf{S}$, where S denotes the rate-of-strain tensor. This prevalent alignment was speculated to be a universal feature of the geometrical structures in 3D turbulence [10]. By retrieving similar aspects at Ra $= 10^{11}$, Fig. 3 shows the PDF of $\cos(\boldsymbol{\omega}, \boldsymbol{\lambda}_i) = (\boldsymbol{\omega} \cdot \boldsymbol{\lambda}_i)/(|\boldsymbol{\omega}||\boldsymbol{\lambda}_i|)$ [Fig. 3(a)] and $\cos(\boldsymbol{\omega}, \boldsymbol{\omega}\mathsf{S})$ [Fig. 3(b)], plotted together with the previous outcomes of turbulent RBC cases through the bulk. The present case indicates similar trends and manifestation on the universal positiveness of the net enstrophy production, i.e., $\langle \boldsymbol{\omega} \cdot \boldsymbol{\omega}\mathsf{S}\rangle > 0$ [18], which is revealed in Fig. 3(b). It is worth noting that the present aspects, inspected in Figs. 2 and 3 at Ra $= 10^{11}$, are very similar to those at Ra $= 10^{10}$ [18].

III. EVOLUTION IN A 3D PHASE SPACE

Principally, in the present work, we seek to expose the role of strain generation $R_\mathsf{S} = -1/3\,\mathrm{tr}(\mathsf{S}^3)$ and enstrophy production $\mathrm{tr}(\Omega^2\mathsf{S}) = R_\mathsf{S} - R_\mathsf{G}$ in controlling the evolution of small-scale dynamics, where $\mathsf{S} = 1/2(\mathsf{G} + \mathsf{G}^t)$ and $\Omega = 1/2(\mathsf{G} - \mathsf{G}^t)$ are the rate-of-strain and rate-of-rotation tensors, respectively. To do so, we expand our 2D $(Q_\mathsf{G}, R_\mathsf{G})$ evolution study [18] to the 3D phase space $(Q_\mathsf{G}, R_\mathsf{S}, R_\mathsf{S} - R_\mathsf{G})$ by decomposing $R_\mathsf{G} = R_\mathsf{S} - \mathrm{tr}(\Omega^2\mathsf{S})$ into its two components, similar to Lüthi *et al.* [30]. In this way, we avoid the planner projection of trajectories onto $(Q_\mathsf{G}, R_\mathsf{G})$; therewith the influence of increasing turbulence (nonlinearity) is difficult to distinguish [18]. In other words, we better disclose the local self-amplification nature of G at high Ra in the evolution of flow topology

by separating the production terms, i.e., R_S and $\mathrm{tr}(\Omega^2 S)$, which were blended to R_G in the (Q_G, R_G) space [10,18]. These third-moment nonlinearities are essential parts of the enstrophy $\boldsymbol{\omega}^2$ and total strain S^2 transport equations. Namely, by taking the gradient of the NS equations (1) and using the definition of the invariants $Q_\Omega = -1/2\,\mathrm{tr}(\Omega^2) = 1/4|\boldsymbol{\omega}|^2$ and $Q_S = -1/2\,\mathrm{tr}(S^2)$, these transport equations read

$$\frac{DQ_S}{Dt} = -3R_S + \mathrm{tr}(\Omega^2 S) - \mathrm{tr}(SH_S), \tag{4}$$

$$\frac{DQ_\Omega}{Dt} = 2\,\mathrm{tr}(\Omega^2 S) - \mathrm{tr}(\Omega H_\Omega), \tag{5}$$

where

$$H_S = -\left(H(p) - \frac{2Q_G}{3}I\right) + \sqrt{\frac{\mathrm{Pr}}{\mathrm{Ra}}}\nabla^2 S + 1/2(\boldsymbol{\nabla f} + \boldsymbol{\nabla f}^t), \tag{6}$$

$$H_\Omega = \sqrt{\frac{\mathrm{Pr}}{\mathrm{Ra}}}\nabla^2 \Omega + 1/2(\boldsymbol{\nabla f} - \boldsymbol{\nabla f}^t) \tag{7}$$

are second-order tensors that include the terms of the resultant pressure Hessian $H(p)$, the viscous diffusion terms of strain $(\mathrm{Pr}/\mathrm{Ra})^{1/2}\nabla^2 S$ and rotation $(\mathrm{Pr}/\mathrm{Ra})^{1/2}\nabla^2\Omega$, and the gradient of the buoyancy forces ∇f. On the other hand, it is worth recalling that this 3D phase space is a subset of the 5D phase space of invariants $(Q_G, R_G, Q_S, R_S, V^2)$ that fully describes the local flow topology for incompressible flows [14] and composes the cornerstone of turbulence models [31]. For the so-called restricted Euler (RE) equations (where the pressure, viscosity, and buoyancy terms are neglected), the transport equations of these invariants read [14,31]

$$\frac{DQ_G}{Dt} = -3R_G, \quad \frac{DR_G}{Dt} = \frac{2}{3}Q_G^2, \tag{8}$$

$$\frac{DQ_S}{Dt} = -2R_S - R_G, \quad \frac{DR_S}{Dt} = \frac{2}{3}Q_G Q_S + \frac{1}{4}V^2, \quad \frac{DV^2}{Dt} = -\frac{16}{3}(R_S - R_G)Q_G, \tag{9}$$

where $V^2 = 4[\mathrm{tr}(S^2\Omega^2) - 2Q_S Q_\Omega] = |S\boldsymbol{\omega}|^2 \geqslant 0$ is the L^2-norm of vortex-stretching vector.

Identically to the 2D evolution procedure adopted in Refs. [15,18], the conditional 3D phase space $(Q_G, R_S, R_S - R_G)$ is analyzed using data from the bulk region $[V_{\mathrm{bulk}} = \{\boldsymbol{x} = (x, y, z) | 0.2 \leqslant y \leqslant 0.8; 0.2 \leqslant z \leqslant 0.8\}]$ and dividing the domain

$$\left\{\begin{array}{c} -2 \leqslant Q_G/\langle Q_\Omega\rangle \leqslant 2 \\ -0.2 \leqslant R_S/\langle Q_\Omega\rangle^{3/2} \leqslant 1.2 \\ -1 \leqslant (R_S - R_G)/\langle Q_\Omega\rangle^{3/2} \leqslant 1 \end{array}\right\}$$

into $40 \times 40 \times 40$ bins. Therein, the average approach to the material derivative of Q_G, R_S, and $R_S - R_G$ is applied conditionally upon the invariants themselves. Namely, using a set of consecutive instantaneous flow fields collected during ζ_{st} (see Table I), the three components

$$\left\langle \frac{DQ_G}{Dt} \middle| -\frac{1}{2} \leqslant \frac{(Q_G - Q_G^0)}{\Delta Q_G} < \frac{1}{2}; -\frac{1}{2} \leqslant \frac{(R_S - R_S^0)}{\Delta R_S} < \frac{1}{2}; -\frac{1}{2} \leqslant \frac{(R_S - R_G) - (R_S^0 - R_G^0)}{\Delta(R_S - R_G)} < \frac{1}{2} \right\rangle,$$

$$\left\langle \frac{DR_S}{Dt} \middle| -\frac{1}{2} \leqslant \frac{(Q_G - Q_G^0)}{\Delta Q_G} < \frac{1}{2}; -\frac{1}{2} \leqslant \frac{(R_S - R_S^0)}{\Delta R_S} < \frac{1}{2}; -\frac{1}{2} \leqslant \frac{(R_S - R_G) - (R_S^0 - R_G^0)}{\Delta(R_S - R_G)} < \frac{1}{2} \right\rangle,$$

$$\left\langle \frac{D(R_S - R_G)}{Dt} \middle| -\frac{1}{2} \leqslant \frac{(Q_G - Q_G^0)}{\Delta Q_G} < \frac{1}{2}; -\frac{1}{2} \leqslant \frac{(R_S - R_S^0)}{\Delta R_S} < \frac{1}{2}; -\frac{1}{2} \leqslant \frac{(R_S - R_G) - (R_S^0 - R_G^0)}{\Delta(R_S - R_G)} < \frac{1}{2} \right\rangle \tag{10}$$

are computed to compose 3D vectors, where $(Q_G^0, R_S^0, R_S^0 - R_G^0)$ are the center coordinates of the bin size $(\Delta Q_G, \Delta R_S, \Delta(R_S - R_G))$. A robust converging of the rates therein has been accomplished

using a high number of samples (greater than 1000) per bin. The mean rate vectors are integrated along some paths to produce the conditional mean trajectories (CMTs) for the three turbulent cases $\mathrm{Ra} = \{10^8, 10^{10}, 10^{11}\}$ displayed in Figs. 4(a)–4(c), respectively.

With close inspection, one can deduce the following 3D scenario of dynamics in the mean: At $\mathrm{Ra} = 10^8$, the evolution of flow topology seems to be very weak in areas dominated by high positive values of strain production $R_S > 0$. This consistently corresponds with the prevalence of the tubelike rotational geometry over strain slots in the bulk at that turbulent grade [18]. Therefore, the CMTs follow a planer (Q_G, R_G) rotation near $R_S = 0$ moving on average from strain-dominated regions [Vieillefosse tail [32] at the null-discriminant plane $D_G = 0$ where $Q_G < 0$ and R_S dominates $\mathrm{tr}(\Omega^2 \mathsf{S})$] towards the enstrophy-dominated areas $Q_G > 0$ of vortex stretching $R_S - R_G > 0$ to regions of vortex contraction $R_S - R_G < 0$ and so on [see Fig. 4(a)]. They finally decay towards the origin (0,0,0), vanishing the fluctuations in the mean and leaving the large scales of the coherent uniform flow next to the origin [18].

By increasing the Ra number, the trajectories' movement is drastically expanded to 3D helical tracks. They start the rotation in regions dominated by vortex stretching $R_S - R_G > 0$ and strain production $R_S > 0$ preferentially located in strain-dominated areas $-Q_S$ or $Q_G < 0$ [see the facing Q_G-R_S plane of combined CMTs for all cases, shown in Fig. 4(f)]. This helical movement becomes notable, stronger, and further developed at $\mathrm{Ra} = \{10^{10}, 10^{11}\}$ [see Figs. 4(b) and 4(c), respectively]. It manifests in (i) the enhanced *local* interaction $\boldsymbol{\omega}/\mathsf{S}$, which amplifies the linear contribution of vortex stretching in strain-dominated slots. Nearby observations suggest that the axis of this helical behavior begins to be perpendicular to the intersection line of the $Q_G = 0$ and $D_G = 0$ tent plane, in very high positive values of $R_S - R_G$ and R_S [see Fig. 4(d) and the facing R_S-$(R_S - R_G)$ plane in Fig. 4(e)]. Afterward, closer to the origin, the CMTs reverse their clockwise roll when they run downward below, after crossing the $D_G = 0$ tent plane [see Figs. 4(d) and 4(f)], and return to their original rotation after flowing upward, rotating towards the origin with an axis normal to the Q_G-$(R_S - R_G)$ plane near $R_S = 0$. This directional modification in the strain-dominated regions $-Q_S$ is due to the opposite sign of R_S and $\mathrm{tr}(\Omega^2 \mathsf{S})$ inside Eq. (4).

While approaching the end, the vectors of mean dynamics obey a rapid downward action in areas of enstrophy domination $Q_G > 0$, vortex contraction $R_S - R_G < 0$, and strain production $R_S > 0$. This action becomes stronger when increasing the turbulence grade, i.e., with higher Ra [see vectors in Figs. 4(a)–4(c), plotted by length and color range proportional to their magnitude]. Relevant CMTs are found to travel extensively downward in the strain-dominated areas $Q_G < 0$ towards high values of $R_S > 0$ as the Ra increases [see Figs. 4(a)–4(c) and 4(f); for a better grasp of the evolution, see the movie of the CMTs for $\mathrm{Ra} = 10^{10}$ in Ref. [33]]. This in turn confirms two additional issues: (ii) A local self-amplification of the turbulence background G and viscous straining $-Q_S$ in growing strain-dominated areas takes place at hard turbulent RBC and corresponds to amplified vorticity contracting events [note that positive values of R_S and negative ones of $\mathrm{tr}(\Omega^2 \mathsf{S})$ strengthen $-Q_S$ and vice versa in Eq. (4)] and (iii) there is a direct and local collaborative role of vortex compression in the dissipative actions and kinetic energy cascade. That is, vortex compression $R_S - R_G < 0$ aids the production of strain and dissipation $R_S > 0$ and the kinetic energy cascade, on the contrary to the vortex stretching that suppresses the cascade [10].

In order to certify conclusion (i), we investigate the local underlying physics of the vortex-stretching vector $\boldsymbol{\omega}\mathsf{S}$. Namely, we propose to evaluate the mean value distribution of the squared magnitude of the vortex-stretching vector, i.e., V^2, conditioned on the joint PDF map of $(Q_G, R_S - R_G)$ invariants. By doing so, we can determine whether the highest stretching pertains to the enstrophy-dominated Q_Ω regions or the strain-dominated $-Q_S$ regions. Hence, the average values $\langle V^2 | (Q_G, R_S - R_G) \rangle$, which are conditioned by the most probable joint PDF of Q_G and $(R_S - R_G)$ in their own space, are plotted and shown in Fig. 5(a) for $\mathrm{Ra} = 10^8$. As expected, even at the lowest turbulent case $\mathrm{Ra} = 10^8$, the maximum mean V^2 (black circle) is located in the positive enstrophy production $R_S - R_G > 0$ and strain-dominated $Q_G < 0$ areas. Although the enstrophy production and V^2 remain large in the rotation-dominated Q_Ω regions, its highest order of magnitude occur in the strain-dominated slots. Similar pictures are observed for the higher Ra numbers, identified by

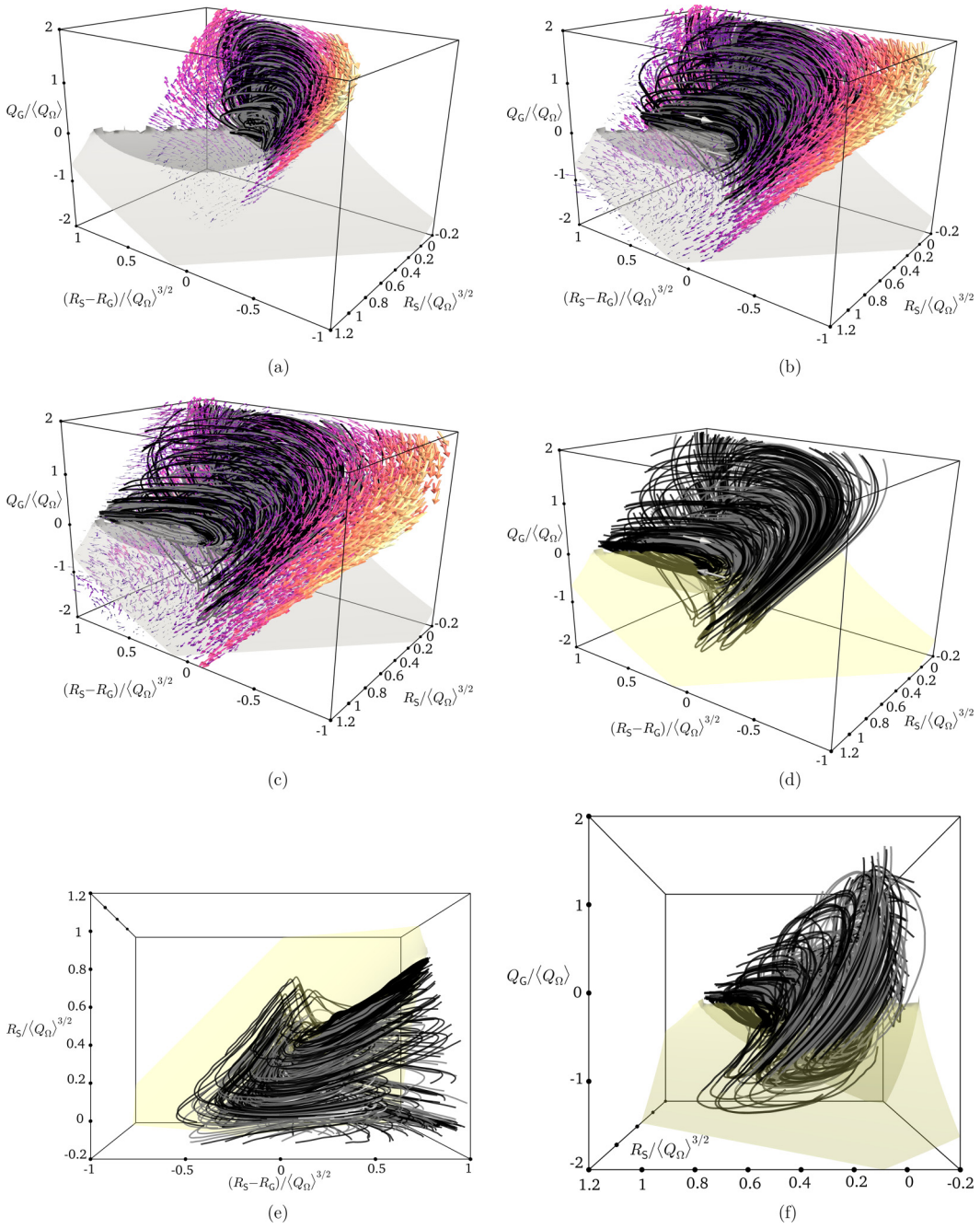

FIG. 4. Conditional mean vectors ($\langle DQ_G/Dt\rangle$, $\langle DR_S/Dt\rangle$, $\langle D(R_S - R_G)/Dt\rangle$) in ($Q_G$, R_S, $R_S - R_G$) space, colored and scaled proportionally to their magnitudes and plotted together with their integral trajectories (black and gray lines) at (a) Ra $= 10^8$, (b) 10^{10}, and (c) 10^{11}, through V_{bulk}. (d) Combination of (a)–(c) trajectories, plotted together in clear gray for Ra $= 10^8$, dark gray for Ra $= 10^{10}$, and black for Ra $= 10^{11}$. Also shown representations of (d) in (e) R_S-($R_S - R_G$) and (f) Q_G-R_S facing views. The transparent tent-shaped surface in all figures indicates the null-discriminant surface $D_G = \frac{27}{4}R_G^2 + Q_G^2 = 0$.

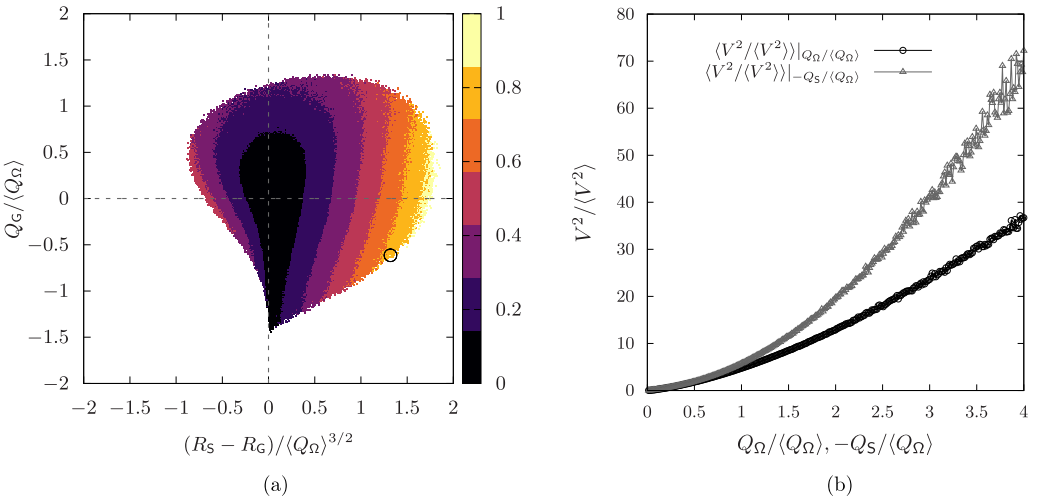

FIG. 5. (a) Average squared magnitude of the vortex-stretching vector i.e., $\langle V^2\rangle$, conditioned on $(Q_G, R_S - R_G)$ invariant space and normalized by its maximum. (b) Conditional averages of V^2 in slots of Q_Ω and $-Q_S$. The data set analyzed in both figures is obtained from $\mathrm{Ra} = 10^8$ through the bulk, where the small black circle in (a) points out the maximum magnitude.

higher magnitudes for all elements. For a sharper comparison, the conditional averages of V^2 are determined (separated) in slots of Q_Ω and $-Q_S$, as displayed in Fig. 5(b), meaning that we compute the mean value of $\langle V^2/\langle V^2\rangle\rangle$ in each bin $\Delta Q_\Omega/\langle Q_\Omega\rangle$ and $-\Delta Q_S/\langle Q_\Omega\rangle$, which make up a total number of 300 bins. Again, for $\mathrm{Ra} = 10^8$ (similar to the others), the stretching magnitude is much larger in strain-dominated areas than that in enstrophy-dominated ones and the main contribution to the vortex stretching in these regions comes from effects associated with the local interaction $\boldsymbol{\omega}/\mathsf{S}$. These findings, in particular the clear evidence in Fig. 5(b), are consistent with those in Ref. [34], where DNS results in a box with periodic boundary conditions at $\mathrm{Re}_\lambda = 75$ were used.

More investigations conducted for the same term V^2, but conditioned on the Q_Ω and $-Q_S$ joint PDF map, are shown in Fig. 6. This map provides physical information about the dominant flow topologies with respect to the kinetic energy dissipation. For example, points of high enstrophy Q_Ω but very small dissipation $-Q_S$ indicate solid-body rotational structures (vortex tubes), while points of strong dissipation but little enstrophy represent irrotational straining domination. A balanced distribution of $Q_\Omega = -Q_S$ translates into a vortex sheet topology, which normally occurs in the BLs. It was found in Ref. [18] that the bulk geometries are mainly tubelike rotational with a map skewed towards high Q_Ω at $\mathrm{Ra} = 10^8$ [Fig. 6(a)]. However, at $\mathrm{Ra} = 10^{10}$, the self-growth of $-Q_S$ geometries was clearly identified, as demonstrated in Fig. 6(b). If we plot the average values of $\langle V^2|(Q_\Omega, -Q_S)\rangle$, similar to Fig. 5(a), it can be observed that at $\mathrm{Ra} = 10^8$ the maximum value (black circle) lies at $-Q_S \sim 0.7$ in the dominated rotational topologies. This is natural since the vortex stretching obeys a dominant long-lived solid-body rotation. Note also the same maximum position of average V^2 at $Q_G \sim -0.7$ in Fig. 5(a). When the turbulence grade increases ($\mathrm{Ra} = 10^{10}$, which has the same trends as $\mathrm{Ra} = 10^{11}$), the vortex tubes break up by developing local (self-amplified) straining in the stretching contributions, and the maximum $\langle V^2|(Q_\Omega, -Q_S)\rangle$ shifts upward in Fig. 6(b), towards higher values of $-Q_S$. All these events confirm conclusions (i) and (ii).

Our resultant evolution is consistent, to some extent, with the evolution dynamics studied by Lüthi *et al.* [30] for isotropic turbulence in the same 3D phase space. They found the same cyclical evolution in areas of positive enstrophy and strain productions, with the same rotation axis, leading to enstrophy-dominated regions $Q_G > 0$. It is noteworthy to evoke the statistical comparable aspects of isotropic turbulence with the bulk structures of RBC at $\mathrm{Ra} = 10^8$, as shown in Ref. [18]. Therein,

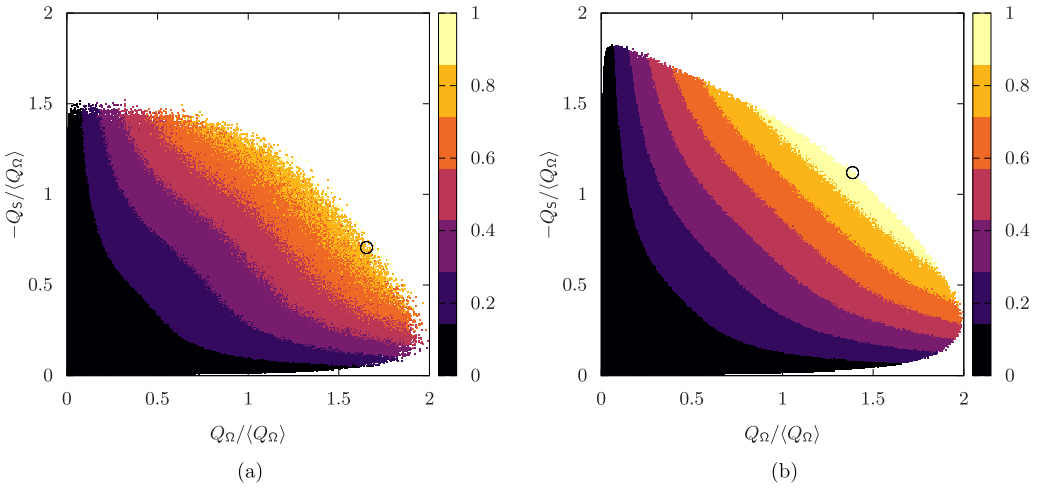

FIG. 6. Average squared magnitude of the vortex-stretching vector, i.e., $\langle V^2 \rangle$, conditioned on $(Q_\Omega, -Q_S)$ invariant space and normalized by its maximum. The statistics analyzed are taken from (a) $\mathrm{Ra} = 10^8$ and (b) $\mathrm{Ra} = 10^{10}$ through the bulk. Similar to Fig. 5(a), the small black circle indicates the maximum value of $\langle V^2 \rangle$.

the joint PDF map of $(Q_\Omega, -Q_S)$, in V_{bulk}, was found to be of similar distribution as the forced isotropic turbulence investigated in Ref. [15]. However, at higher Rayleigh number $\mathrm{Ra} = 10^{10}$, the distribution deviates [Fig. 6(b)]. Hence, such a discrepancy with respect to the results obtained in Ref. [30] for isotropic turbulence may be produced by our higher turbulence grades, the confinement effect of our RBC, and the different mechanism of injecting kinetic energy into the system, i.e., by the dissipation of thermal plumes.

For a rough comparison, we have simulated the evolution of the 5D phase space of invariants $(Q_G, R_G, Q_S, R_S, V^2)$ for the RE equations projected onto our 3D phase space $(Q_G, R_S, R_S - R_G)$. To do so, we have integrated Eqs. (8) and (9) explicitly from multiple initial values for $(Q_G, R_G, Q_S, R_S, V^2)$, and their evolution has been projected and plotted in the 3D phase space $(Q_G, R_S, R_S - R_G)$ in Fig. 7(a) together with the tent plane $D_G = 0$. We note how the trajectories start from small values of $R_S - R_G > 0$ and $R_S > 0$ in the strain-dominated regions $Q_G < 0$ and asymptotically approach the left-hand side of the $D_G = 0$ wire mesh. Then they expand and rotate in the quadrant of positive enstrophy and strain productions $R_S - R_G > 0$ and $R_S > 0$ towards high values in the rotation-dominated areas $Q_G > 0$ [see Figs. 7(a) and 7(b)]. This behavior is similar to the dynamics observed in the DNS [see Fig. 4(e), where the rotation axis is similar to that in Fig. 7(b)], but the spiraling direction is reversed and is preferentially located in strain-dominated areas $Q_G < 0$ [see Fig. 4(f)]. It can be deduced that at a high turbulence grade, the effect of the nonlinear advection (convective term) appears in both cases and concentrates, for the RE model, in the centered vorticity tubelike filaments or worms, where the vortex stretching and intensive enstrophy are dominant, i.e., $R_S - R_G > 0$, $Q_G > 0$, and $R_S > 0$. In particular, in these areas where Q_Ω is dominant, for the DNS the enstrophy production is in an approximate balance with the viscous destruction of rotation $-\mathrm{tr}[\Omega(\mathrm{Pr}/\mathrm{Ra})^{1/2}\nabla^2\Omega]$, as discussed by Tsinober [10]. Hence, the influence of the natural turbulence remains predominantly in the strain-dominated regions of the vortex-stretching patterns (i), and is primarily returned to the pressure Hessian term. This conforms well with the results of Tsinober *et al.* [34], who found that in regions of high strain the pressure Hessian even enhances the growth of stretching. On the other hand, Lüthi *et al.* [30], in their similar 3D phase space for isotropic turbulence, and other detailed studies [35,36] have corroborated that the RE dynamics is essentially counteracted by the deviatoric nonlocal part of the pressure Hessian and not by the viscous term. Afterward, the RE trajectories continue asymptotically to the right-hand

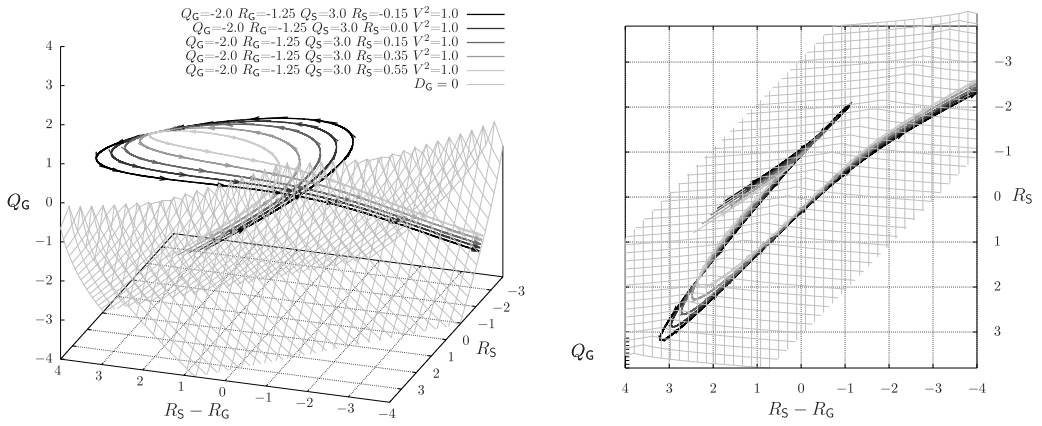

FIG. 7. Evolution trajectories of the 5D phase-space invariants (Q_G, R_G, Q_S, R_S, V^2), given in Eqs. (8) and (9) for the restricted Euler model, plotted together with their vectors in the 3D phase space (Q_G, R_S, $R_S - R_G$). One track (solution) is generated for each set of initial values for the 5D phase space of invariants. The null-discriminant $D_G = 0$ wire-mesh plane is drawn therewith. The trajectories are displayed in two views: (a) from the side and (b) from the top.

side of $D_G = 0$ wire mesh, towards negative values of $R_S < 0$, since negative enstrophy production $\mathrm{tr}(\Omega^2 S) < 0$ leads to negative values of Q_G in its evolution equation [first of Eqs. (8)] with $R_S < 0$. In the DNS, all CMTs are twisted towards $R_S > 0$ to be converged to the origin in a cyclic evolution.

IV. EVOLUTION IN A KINETIC-THERMAL 2D PHASE SPACE

To study the turbulent heat flux and buoyant production mechanisms in turbulent RBC, the small-scale dynamics relevant to thermals was also reported in Ref. [18], for $\mathrm{Ra} = \{10^8, 10^{10}\}$. Namely, we applied the same approach as in the 2D phase space (Q_G, R_G) but using the invariants of the traceless part of the (velocity) × (temperature) gradient tensor, i.e., ($Q_{\tilde{G}_\theta}$, $R_{\tilde{G}_\theta}$), where $\tilde{G}_\theta = G_\theta - 1/3\,\mathrm{tr}(G_\theta)I$, with $G_\theta = \nabla(\boldsymbol{u}T)$. The invariants proposed therein demonstrated a direct picture on the small-scale kinetic-thermal interaction dynamics and thermal plumes evolution in RBC. For example, the statistical analysis of the joint PDF map ($Q_{\tilde{G}_\theta}$, $R_{\tilde{G}_\theta}$), through the total domain, held a symmetric aspect respect to $R_{\tilde{G}_\theta} = 0$ (somewhat similar to a Gaussian flow field) that directly follows the universal log-normal statistics distribution of the thermal plume geometries. It was noted that the CMTs of ($\langle DQ_{\tilde{G}_\theta}/Dt\rangle$, $\langle DR_{\tilde{G}_\theta}/Dt\rangle$) travel downward to expose the sheetlike plumes dynamics (roots) within the BLs and upward to exhibit the evolution of mushroomlike plumes that expands in the bulk. At $\mathrm{Ra} = 10^8$, the trajectories showed two skew-symmetric converging origins, which indicated the contribution of the hot and cold mushroomlike plumes, into the large coherent scales of heat flux. However, at $\mathrm{Ra} = 10^{10}$ the CMTs were traveling upward in shorter tracks to demonstrate the reduced lifetime of mushroomlike plumes under the influence of the self-amplified dissipation and hard mixing. In consequence, all trajectories showed a zero-value converging origin in that turbulent case. In this work, we have extended the range up to $\mathrm{Ra} = 10^{11}$ (results are shown in Fig. 8). Similar to $\mathrm{Ra} = 10^{10}$, we have noticed the zero-value converging origin of CMTs plotted across the whole domain [Fig. 8(a)] and a similar joint PDF ($Q_{\tilde{G}_\theta}$, $R_{\tilde{G}_\theta}$) distribution with increasing events (points) located below $D_{\tilde{G}_\theta} = 0$ [Fig. 8(b)]. This confirms our previous findings that the mushroomlike thermal plumes are abundantly emitted in the BLs and scattered in the bulk under the impact of self-amplified turbulence background. Hence, they do not contribute to the mean (large-scale) heat flux as well at $\mathrm{Ra} = 10^{11}$. However, a very interesting feature can be drawn, namely, the evolution of sheetlike plumes vanishes at the expense of increasing the evolution of

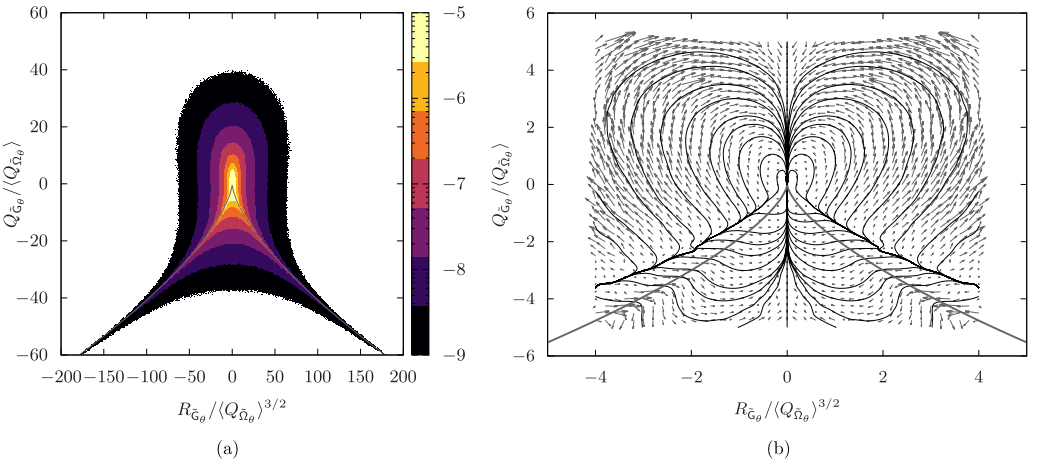

FIG. 8. Same representation as in Fig. 2 considering (a) the joint PDF of $(Q_{\tilde{\mathsf{G}}_\theta}, R_{\tilde{\mathsf{G}}_\theta})$ and (b) $\langle DQ_{\tilde{\mathsf{G}}_\theta}/Dt\rangle$ and $\langle DR_{\tilde{\mathsf{G}}_\theta}/Dt\rangle$ in the $(Q_{\tilde{\mathsf{G}}_\theta}, R_{\tilde{\mathsf{G}}_\theta})$ space. The results correspond to the RBC simulation at $\mathrm{Ra} = 10^{11}$ through the total domain. The gray solid line in (a) and (b) represents $D_{\tilde{\mathsf{G}}_\theta} = 0$.

mushroomlike plumes at $\mathrm{Ra} = 10^{11}$. This has been deduced from the total upward tracks of CMTs below the null-discriminant curve $D_{\tilde{\mathsf{G}}_\theta} = 0$ at $Q_{\tilde{\mathsf{G}}_\theta} < 0$ [see Fig. 8(b)]. They arise as a true reflection of the increased emitting mushroomlike plumes in the BLs and the placements of more events below $D_{\tilde{\mathsf{G}}_\theta} = 0$ in Fig. 8(a). It was found in Ref. [18] that $D_{\tilde{\mathsf{G}}_\theta} = 0$ curve can separate the sheetlike plumes' (roots') evolution (which move downward at $\mathrm{Ra} = \{10^8, 10^{10}\}$ below $D_{\tilde{\mathsf{G}}_\theta} = 0$) in the BLs, from the arisen mushroomlike plumes expanded into the bulk (which move upward above $D_{\tilde{\mathsf{G}}_\theta} = 0$ and converge to the origin). Accordingly, this event supports the fact that the horizontal waves, which travel in the BLs and interact with each other to compose the sheetlike plumes [37], become *weaker* at $\mathrm{Ra} = 10^{11}$. In other words, fewer *stabilizing* effects are pronounced in the BLs, which become even thinner at $\mathrm{Ra} = 10^{11}$ and tend to lose their laminar status.

V. CONCLUSION

On the basis of a fully resolved DNS data set for an air buoyancy-driven RBC, the behavior of the small-scale dynamics inside the bulk region has been explored in different turbulent regimes $\mathrm{Ra} = \{10^8, 10^{10}, 10^{11}\}$. By adopting an approach similar to that of Lüthi *et al.* [30], we have expanded the 2D Lagrangian evolution of Q_{G} and R_{G} invariants, previously reported in Ref. [18], to a 3D phase space by decomposing R_{G} into two parts: the strain production R_{S} and the enstrophy production $\mathrm{tr}(\Omega^2\mathsf{S})$. By doing so, we have demonstrated the existence of a 3D cyclical evolution of the G state, strongly expanded for the hard turbulent cases, i.e., $\mathrm{Ra} = \{10^{10}, 10^{11}\}$. This cyclical rotation starts preferentially in the strain-dominated areas from regions of high positive magnitudes of vortex stretching and strain production. Following its life cycle, the concluded outcomes manifest a rising self-amplification of G in the strain-dominated area, as the turbulence grade increases. This process is accompanied by a strong enhanced vortex contraction and amplified linear contributions of vortex stretching, which are particularly related to the strain-dominated slots. Regarding the evolution of the small-scale thermals, the 2D evolution of $Q_{\tilde{\mathsf{G}}_\theta}$ and $R_{\tilde{\mathsf{G}}_\theta}$, invariants of $\tilde{\mathsf{G}}_\theta = \mathsf{G}_\theta - 1/3\,\mathrm{tr}(\mathsf{G}_\theta)\mathsf{I}$, with $\mathsf{G}_\theta = \boldsymbol{\nabla}(\boldsymbol{u}T)$, was investigated for first time in Ref. [18], at $\mathrm{Ra} = \{10^8, 10^{10}\}$, showing a direct description of thermal plume evolution in RBC. Here it has been extended by considering the case at $\mathrm{Ra} = 10^{11}$. In this turbulent regime, we have noticed a clear tendency to reduce the evolution of sheetlike plumes in the BLs at the expense of the increasing emission of mushroomlike plumes. This may support the fact that a reduced laminarization of the BL occurs at $\mathrm{Ra} = 10^{11}$.

It would be of great interest to extend this analysis to even higher Rayleigh numbers, especially up to the point where BLs reach a turbulent regime. However, nowadays, DNS of buoyancy-driven flows is still limited to relatively low Rayleigh numbers because the convective term produces far too many relevant scales of motion. Therefore, it would be valuable to research the development of better subgrid heat flux models in large-eddy simulation.

ACKNOWLEDGMENTS

F.X.T., F.D., and A.O. were financially supported by the Ministerio de Economía y Competitividad, Spain (Grant No. ENE2017-88697-R). F.X.T. was supported by the Ramón y Cajal postdoctoral program (Contract No. RYC-2012-11996). F.D. was supported by the Austrian Federal Ministry for Digital and Economic Affairs, the National Foundation for Research, Technology and Development, and the K1-MET GmbH, metallurgical competence center. The research program of the K1-MET competence center is supported by COMET (Competence Center for Excellent Technologies), the Austrian program for competence centers. COMET is funded by the Federal Ministry for Transport, Innovation and Technology, the Federal Ministry for Digital and Economic Affairs and the provinces of Upper Austria, Tyrol and Styria, and, beside the public funding from COMET, by the industrial partners Primetals Technologies Austria GmbH, voestalpine Stahl Donawitz GmbH, RHI Magnesita GmbH and voestalpine Stahl GmbH. Calculations were performed on the MareNostrum 4 supercomputer at the Barcelona Supercomputing Center (PRACE 15th Call, Ref. 2016163972, "Exploring new frontiers in Rayleigh-Bénard convection"). Preliminary simulations were obtained using computational resources of MCC NRC "Kurchatov Institute" [38]. The authors gratefully acknowledge these institutions.

[1] F. Chillà and J. Schumacher, New perspectives in turbulent Rayleigh-Bénard convection, Eur. Phys. J. E **35**, 58 (2012).

[2] G. Ahlers, S. Grossmann, and D. Lohse, Heat transfer and large scale dynamics in turbulent Rayleigh-Bénard convection, Rev. Mod. Phys. **81**, 503 (2009).

[3] E. D. Sigga, High Rayleigh number convection, Annu. Rev. Fluid Mech. **26**, 137 (1994).

[4] R. Togni, A. Cimarelli, and E. D. Angelis, Physical and scale-by-scale analysis of Rayleigh-Bénard convection, J. Fluid Mech. **782**, 380 (2015).

[5] K. Hanjalić, One-point closure models for buoyancy-driven turbulent flows, Annu. Rev. Fluid Mech. **34**, 321 (2002).

[6] G. Amati, K. Koal, F. Massaioli, K. R. Sreenivasan, and R. Verzicco, Turbulent thermal convection at high Rayleigh numbers for a Boussinesq fluid of constant Prandtl number, Phys. Fluids **17**, 121701 (2005).

[7] R. A. J. M. Stevens, R. Verzicco, and D. Lohse, Radial boundary layer structure and Nusselt number in Rayleigh-Bénard convection, J. Fluid Mech. **643**, 495 (2010).

[8] R. J. A. M. Stevens, D. Lohse, and R. Verzicco, Prandtl and Rayleigh number dependence of heat transport in high Rayleigh number thermal convection, J. Fluid Mech. **688**, 31 (2011).

[9] E. P. van der Poel, R. Verzicco, S. Grossmann, and D. Lohse, Plume emission statistics in turbulent Rayleigh- Bénard convection, J. Fluid Mech. **772**, 5 (2015).

[10] A. Tsinober, *An Informal Introduction to Turbulence* (Kluwer Academic, Dordrecht, 2001), Vol. 63.

[11] H. Tennekes and J. L. Lumley, *A First Course in Turbulence* (MIT Press, Cambridge, 1972).

[12] K. R. Sreenivasan and R. A. Antonia, The phenomenology of small-scale turbulence, Annu. Rev. Fluid Mech. **29**, 435 (1997).

[13] M. S. Chong, A. E. Perry, and B. J. Cantwell, A general classification of three-dimensional flow fields, Phys. Fluids A **2**, 765 (1990).

[14] J. Martín, A. Ooi, M. S. Chong, and J. Soria, Dynamics of the velocity gradient tensor invariants in isotropic turbulence, Phys. Fluids **10**, 2336 (1998).

[15] A. Ooi, J. Martin, J. Soria, and M. S. Chong, A study of the evolution and characteristics of the invariants of the velocity-gradient tensor in isotropic turbulence, J. Fluid Mech. **381**, 141 (1999).
[16] F. Dabbagh, F. X. Trias, A. Gorobets, and A. Oliva, *A priori* study of subgrid-scale features in turbulent Rayleigh-Bénard convection, Phys. Fluids **29**, 105103 (2017).
[17] R. Togni, A. Cimarelli, and E. D. Angelis, Resolved and subgrid dynamics of Rayleigh-Bénard convection, J. Fluid Mech. **867**, 906 (2019).
[18] F. Dabbagh, F. X. Trias, A. Gorobets, and A. Oliva, On the evolution of flow topology in turbulent Rayleigh-Bénard convection, Phys. Fluids **28**, 115105 (2016).
[19] G. E. Elsinga and I. Marusic, Evolution and lifetimes of flow topology in a turbulent boundary layer, Phys. Fluids **22**, 015102 (2010).
[20] H. M. Blackburn, N. N. Mansour, and B. J. Cantwell, Topology of fine-scale motions in turbulent channel flow, J. Fluid Mech. **310**, 269 (1996).
[21] J. Soria, R. Sondergaard, B. J. Cantwell, M. S. Chong, and A. E. Perry, A study of the fine-scale motions of incompressible time-developing mixing layers, Phys. Fluids **6**, 871 (1994).
[22] C. B. da Silva and J. C. F. Pereira, Invariants of the velocity-gradient, rate-of-strain, and rate-of-rotation tensors across the turbulent/nonturbulent interface in jets, Phys. Fluids **20**, 055101 (2008).
[23] F. X. Trias, F. Dabbagh, A. Gorobets, and C. D. Pérez-Segarra, Exploring new frontiers in Rayleigh-Bénard convection, PRACE Report No. 2016163972, 2017 (unpublished).
[24] A. Gorobets, F. X. Trias, R. Borrell, O. Lehmkuhl, and A. Oliva, Hybrid MPI+OpenMP parallelization of an FFT-based 3D Poisson solver with one periodic direction, Comput. Fluids **49**, 101 (2011).
[25] R. W. C. P. Verstappen and A. E. P. Veldman, Symmetry-preserving discretization of turbulent flow, J. Comput. Phys. **187**, 343 (2003).
[26] F. X. Trias and O. Lehmkuhl, A self-adaptive strategy for the time-integration of Navier-Stokes equations, Numer. Heat Transfer B **60**, 116 (2011).
[27] R. J. A. M. Stevens, E. P. van der Poel, S. Grossmann, and D. Lohse, The unifying theory of scaling in thermal convection: The updated prefactors, J. Fluid Mech. **730**, 295 (2013).
[28] G. Grötzbach, Spatial resolution requirements for direct numerical simulation of the Rayleigh-Bénard convection, J. Comput. Phys. **49**, 241 (1983).
[29] O. Shishkina, R. J. A. M. Stevens, S. Grossmann, and D. Lohse, Boundary layer structure in structure in turbulent thermal convection and consequences for the required numerical resolution, New J. Phys. **12**, 075022 (2010).
[30] B. Lüthi, M. Holzner, and A. Tsinober, Expanding the *Q*-*R* space to three dimensions, J. Fluid Mech. **641**, 497 (2009).
[31] F. X. Trias, D. Folch, A. Gorobets, and A. Oliva, Building proper invariants for eddy-viscosity subgrid-scale models, Phys. Fluids **27**, 065103 (2015).
[32] P. Vieillefosse, Local interaction between vorticity and shear in a perfect incompressible fluid, J. Phys. (Paris) **43**, 837 (1982).
[33] See Supplemental Material at http://link.aps.org/supplemental/10.1103/PhysRevFluids.5.024603 for the conditional mean trajectories of small-scale dynamics in (Q_{G}, R_{S}, tr($\Omega^2\mathsf{S}$)) phase space. The trajectories are plotted for turbulent Rayleigh-Bénard convection at $\mathrm{Ra} = 10^{10}$, in the bulk, and displayed in different facing views.
[34] A. Tsinober, M. Ortenberg, and L. Shtilman, On depression of nonlinearity in turbulence, Phys. Fluids **11**, 2291 (1999).
[35] L. Chevillard, C. Meneveau, L. Biferale, and F. Toschi, Modeling the pressure Hessian and viscous Laplacian in turbulence: Comparisons with direct numerical simulation and implications on velocity gradient dynamics, Phys. Fluids **20**, 101504 (2008).
[36] M. Wilczek and C. Meneveau, Pressure Hessian and viscous contributions to velocity gradient statistics based on Gaussian random fields, J. Fluid Mech. **756**, 191 (2014).
[37] Q. Zhou and K. Q. Xia, Physical and geometrical properties of thermal plumes in turbulent Rayleigh-Bénard convection, New J. Phys. **12**, 075006 (2010).
[38] http://computing.nrcki.ru.